

SPITZER MID-INFRARED UPPER LIMITS ON ANOMALOUS X-RAY PULSARS 1E 1048.1–5937, 1RXS J170849.0–400910, AND XTE J1810–197

ZHONGXIANG WANG¹, VICTORIA M. KASPI¹, AND SARAH J. U. HIGDON^{2,3}

Draft version September 16, 2017

ABSTRACT

We report on mid-infrared imaging observations of the anomalous X-ray pulsars (AXPs) 1E 1048.1–5937, 1RXS J170849.0–400910, and XTE J1810–197. The observations were carried out at 4.5 and 8.0 μ m with the Infrared Array Camera and at 24 μ m with the Multiband Imaging Photometer on the *Spitzer Space Telescope*. No mid-infrared counterparts were detected. As infrared emission from AXPs may be related to their X-ray emission either via the magnetosphere or via a dust disk, we compare the derived upper limits on the infrared/X-ray flux ratios of the AXPs to the same ratio for 4U 0142+61, an AXP previously detected in the mid-infrared range. The upper limits are above the flux ratio for 4U 0142+61, indicating that if AXPs have similar infrared/X-ray flux ratios, our observations were not sufficiently deep to detect our AXP targets. For XTE J1810–197, the upper limits set a constraint on its rising radio energy spectrum, suggesting a spectral break between 4.2×10^{10} and 6×10^{13} Hz.

Subject headings: pulsars: individual (1E 1048.1–5937, 1RXS J170849.0–400910, XTE J1810–197)
 — X-rays: stars — stars: neutron

1. INTRODUCTION

The anomalous X-ray pulsars (AXPs) are a small group of isolated, young neutron stars with spin periods falling in a narrow range (5–12 s), very soft X-ray spectra in the 0.5–10 keV range, and with X-ray burst activity (Woods & Thompson 2006; Kaspi 2007). They were considered “anomalous” because their X-ray luminosities greatly exceed the power available from the rotational kinetic energy of the pulsars. Along with soft gamma-ray repeaters (SGRs), these objects are believed to be neutron stars having extremely strong ($\sim 10^{14}$ G) surface magnetic fields (“magnetars”; Thompson & Duncan 1996).

In addition to studies at X-ray energies, effort has been made to observe AXPs at optical and infrared (IR) wavelengths. Since the discovery of the optical/near-IR counterpart to AXP 4U 0142+61 (Hulleman, van Kerkwijk, & Kulkarni 2000), four other AXPs, 1E 1048.1–5937 (Wang & Chakrabarty 2002), 1RXS J170849.0–400910 (Durant & van Kerkwijk 2006a; Israel et al. 2003), XTE J1810–197 (Israel et al. 2004), and 1E 2259+586 (Hulleman et al. 2001), were also identified in the near-IR. The observed near-IR emission, which greatly exceeds the extrapolated spectrum of the X-ray blackbody component of AXPs, is likely related to the X-ray emission—AXPs show very similar *K*-band to X-ray flux ratios ($1.7\text{--}3.7 \times 10^{-4}$; Durant & van Kerkwijk 2005, 2006a) and correlated near-IR and X-ray flux variations were found for 1E 2259+586 (Tam et al. 2004) and XTE J1810–197 (Rea et al. 2004) during their X-ray outbursts.

In the magnetar model, optical/IR emission is

probably due to non-thermal radiation by particles in the magnetosphere (e.g., Beloborodov & Thompson 2007). However, using the *Spitzer Space Telescope*, Wang, Chakrabarty, & Kaplan (2006) recently identified 4U 0142+61 at the mid-IR wavelengths 4.5 and 8.0 μ m. The emission in the mid-IR was brighter than that in the near-IR, and can be interpreted as dust emission from an X-ray heated passive disk around the young pulsar. Given the similar near-IR fluxes of AXPs, this suggests that AXPs could all be bright at mid-IR wavelengths, due to non-thermal emission from their magnetospheres or the existence of surrounding disks.

In this paper, we report on the *Spitzer* observations of the AXPs 1E 1048.1–5937, 1RXS J170849.0–400910, and XTE J1810–197. The general properties of these three AXPs are summarized in Table 1. We present mid-IR observations in § 2 and our results in § 3. We discuss the implications of our observations in § 4.

2. SPITZER OBSERVATIONS

The fields of three AXPs were observed with *Spitzer* using the Infrared Array Camera (IRAC; Fazio et al. 2004) and Multiband Imaging Photometer for *Spitzer* (MIPS; Rieke et al. 2004), as part of the Infrared Spectrograph (IRS) instrument team guaranteed time program. A summary of the *Spitzer* observations is given in Table 2.

2.1. *Spitzer* IRAC 4.5 and 8.0 μ m Imaging

IRAC is an imaging camera operating in four channels at 3.6, 4.5, 5.8, and 8.0 μ m. Two adjacent fields are simultaneously imaged in pairs (3.6 and 5.8 μ m; 4.5 and 8.0 μ m). We observed our targets in the 4.5 and 8.0 μ m channels, with bandwidths of 1.0 and 2.9 μ m, respectively. The detectors at the short and long wavelengths are InSb and Si:As devices, respectively, with 256×256 pixels and a plate scale of 1''.2, giving a field of view (FOV) of 5.2×5.2 . The frame time was 100 s, with 96.8 s effective exposure time per frame for the 4.5 μ m data

¹ Department of Physics, McGill University, Montreal, QC H3A 2T8, Canada; wangzx@physics.mcgill.ca, vkaspi@physics.mcgill.ca

² Department of Astronomy, Cornell University, Ithaca, NY 14853

³ Department of Physics, Georgia Southern University, Statesboro, GA 30460; shigdon@georgiasouthern.edu

and 93.6 s effective exposure time for the $8.0\text{ }\mu\text{m}$ data. The total exposures of each target's field are given in Table 2.

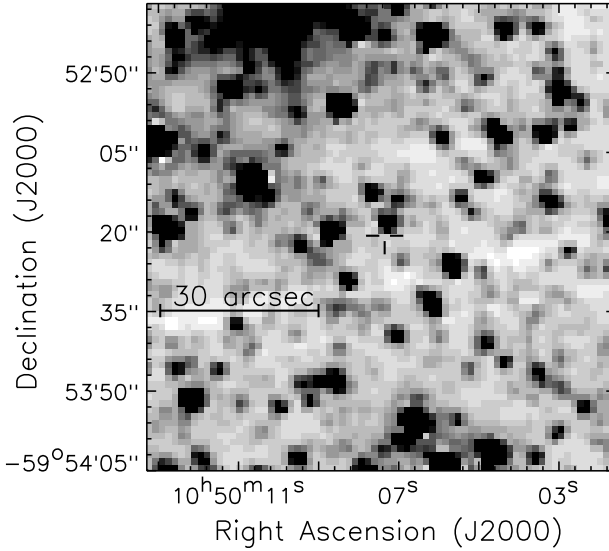


FIG. 1.— *Spitzer* IRAC $4.5\text{ }\mu\text{m}$ image of the 1E 1048.1–5937 field. The source position (Wang & Chakrabarty 2002) is indicated by a cross. No object was found within a $0.^{\prime\prime}5$ radius error circle (too small to be resolved on the images), which is the uncertainty (90% confidence) of locating the near-IR source position in the *Spitzer* images.

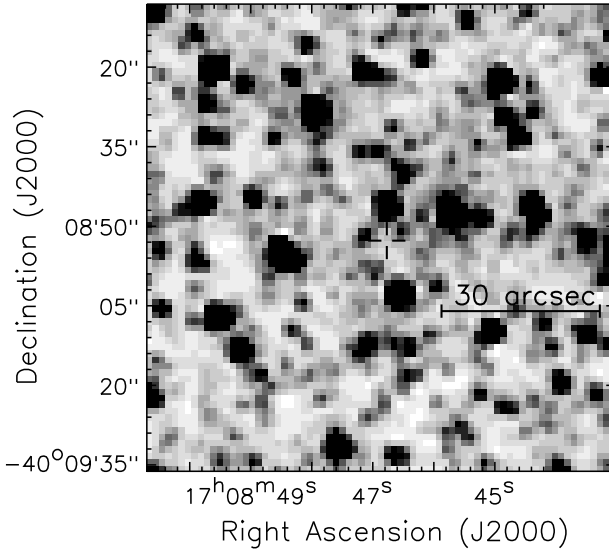


FIG. 2.— *Spitzer* IRAC $4.5\text{ }\mu\text{m}$ image of the 1RXS J170849.0–400910 field. The source position (Israel et al. 2003), with a nominal uncertainty of $0.^{\prime\prime}7$ (90% confidence), is indicated by a cross (the error circle is too small to be resolved on the images).

The data were processed through the data reduction pipelines (version S14.0.0; IRAC Data Handbook, version 3.0, 2006) at the *Spitzer* Science Center. In the basic calibrated data (BCD) pipeline, the individual flux-calibrated frames were produced from the raw images. The BCD frames were then combined into the post-BCD (PBCD) mosaics. The pointing of the IRAC frames is

typically accurate to $0.^{\prime\prime}5$. Because the fields of the AXPs are crowded, we further astrometrically calibrated the PBCD images to achieve the best positional accuracy and avoid source confusion. For the 1E 1048.1–5937, 1RXS J170849.0–400910, and XTE J1810–197 images, 261, 230, and 100 Two Micron All-Sky Survey (2MASS; Skrutskie et al. 2006) stars, detected by each of the $4.5\text{ }\mu\text{m}$ images, were used for the calibrations, respectively. The nominal uncertainties of the calibrated images are dominated by the 2MASS systematic uncertainty ($\simeq 0.^{\prime\prime}15$, with respect to the International Celestial Reference System).

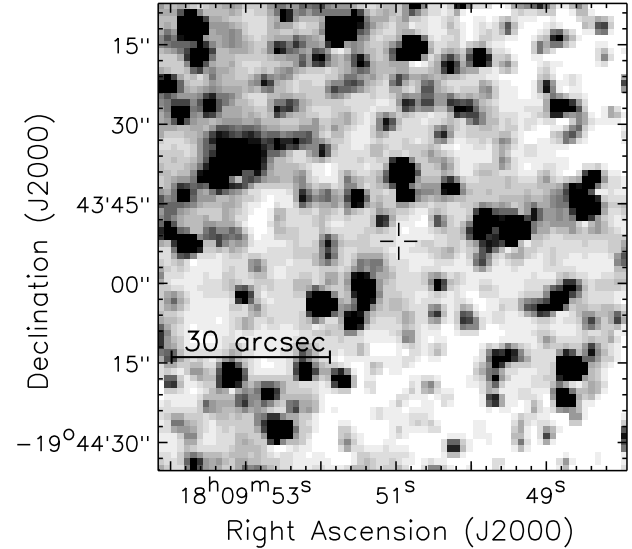


FIG. 3.— *Spitzer* IRAC $4.5\text{ }\mu\text{m}$ image of the XTE J1810–197 field. The *Chandra* source position (Israel et al. 2004) is indicated by a cross. The nominal uncertainty (90% confidence) on the source position is $0.^{\prime\prime}7$. This error circle is too small to be resolved on the images.

2.2. *Spitzer* MIPS 24 μm Imaging

MIPS contains three separate detector arrays which provide capabilities for imaging and photometry in broad bands at 24 , 70 , and $160\text{ }\mu\text{m}$. The $24\text{ }\mu\text{m}$ camera (having $4.7\text{ }\mu\text{m}$ bandwidth) was operated under the Photometry and Super Resolution (PH/SR) mode for the observations. The detector is a 128×128 pixel Si:As array, with a pixel size of $2.^{\prime\prime}55$ and a $5.^{\prime}\times 5.^{\prime}$ FOV. The frame time used was 10-s, with 9.96-s effective exposure time per frame. The total exposure of each source, controlled by the frame time, number of frames per cycle, and number of cycles, is given in Table 2.

The data were processed through the MIPS data reduction pipelines (version S13.2.0; MIPS Data Handbook, version 3.2.1, 2006) at the *Spitzer* Science Center. Similarly to the IRAC data processing, a PBCD image of each target field was produced by the post-BCD pipeline from the BCD images (see MIPS Data Handbook for details).

3. RESULTS

In Figures 1–3, we show the mid-IR images of the 1E 1048.1–5937, 1RXS J170849.0–400910, and XTE J1810–197 fields, respectively. For the first AXP, the source position is from the near-IR observation (Wang & Chakrabarty 2002), while for the latter two,

their *Chandra* X-ray positions (Israel et al. 2003, 2004) were used. Combining the positional uncertainties on the *Spitzer* images and the sources, the 90% confidence radii of the error circles for the AXPs are at $0''.5$ – $0''.7$. In each figure, the source position is indicated by a cross (the error circles are too small to be resolved on the images). No objects were found within the error circle of each source position on the *Spitzer* images. There is one faint object near the position of 1RXS J170849.0–400910, but it is $1''.8$ (or more than 4σ) away from the *Chandra* position.

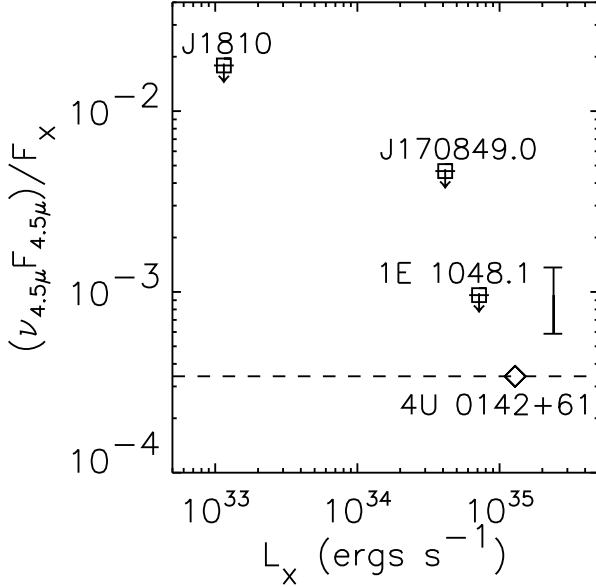


FIG. 4.— Upper limits on the *Spitzer*/IRAC 4.5 μ m to X-ray (in the 2–10 keV range) flux ratios of the three AXPs. Fluxes are unabsorbed, and values of $A_V = 5.6, 7.7$, and 3.6 (derived from N_H by using $A_V = N_H/0.179 \times 10^{22} \text{ cm}^{-2}$; Predehl & Schmitt 1995) are used for dereddening the 4.5 μ m flux upper limits (Indebetouw et al. 2005) of 1E 1048.1–5937, 1RXS J170849.0–400910, and XTE J1810–197, respectively. The dashed line indicates the flux ratio of the AXP 4U 0142+61. The error bar near 1E 1048.1–5937 indicates the uncertainty on its upper limit due to its X-ray variability (Tiengo et al. 2005).

The sensitivity of the IRAC observations is dominated by background sky emission and confusion noise when a field is crowded. The sky brightnesses measured by IRAC and MIPS at our target positions are given in Table 2. As can be seen, 1E 1048.1–5937 has a background between medium to high⁴ (e.g., at 8 μ m, the sky brightness is between 7.7–18.3 MJy/sr). The backgrounds of the other two AXPs are much higher than the high background defined by *Spitzer*, presumably because of their crowded fields. We derived the 3σ flux upper limits from the standard deviation of the background sky at the source positions. The upper limits are given in Table 2.

In addition, we note that for the two objects within the error circle of 1RXS J170849.0–400910 which were both proposed as the possible near-IR counterpart (Israel et al. 2003; Durant & van Kerkwijk 2006a), our IRAC observations would have detected the object A, if we assume that this AXP has the same mid-IR to near-IR flux ratio as that of 4U 0142+61. Therefore, the

non-detection of 1RXS J170849.0–400910 in our IRAC images is also in favor of object B being the near-IR counterpart (Durant & van Kerkwijk 2006a).

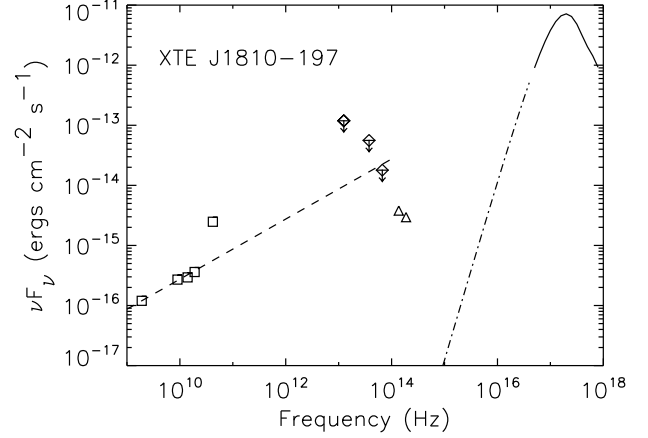


FIG. 5.— Unabsorbed mid-IR flux upper limits for XTE J1810–197 (diamonds). Also shown are its two-blackbody model X-ray flux (solid and dot-dashed curves) from the *XMM* observation on 2005 September 20 (Gotthelf & Halpern 2006), dereddened near-IR H_Ks fluxes (triangles) measured on 2004 March 12–14 (Rea et al. 2004), and radio 1.9, 9.0, 14, 19 (on 2006 May 2) and 42 GHz (on 2006 May 3) fluxes (squares; Camilo et al. 2006). An $S_\nu \propto \nu^{-0.5}$ radio spectrum, which well represents the May-2 data, is indicated by a dashed line.

4. DISCUSSION

As indicated by the similar K -band-to-X-ray flux ratios and the cases of correlated near-IR/X-ray flux variations (although only seen during outbursts), IR emission from AXPs is likely connected to their X-ray emission, either via the magnetosphere or via reprocessing of X-rays by a surrounding dust disk. In the first case, as starquakes shear the external magnetic field, a plasma corona forms in the twisted magnetosphere of a magnetar (Thompson et al. 2002; Beloborodov & Thompson 2007). The observed blackbody component ($kT \sim 0.5$ keV) arises from the atmosphere of this magnetar, which would be partly heated by particles from the corona. The 2–10 keV power-law component is produced by multiple cyclotron scattering of the keV tail of the blackbody by coronal particles. The observed optical/IR emission is probably related to the X-rays, as it may be due to cyclotron or curvature radiation by the particles in the corona (Beloborodov & Thompson 2007). However, currently there is no detailed theoretical model to explain the similar near-IR/X-ray flux ratios in the magnetosphere picture. Alternatively, the IR and X-ray emission may be connected by a dust disk (Wang et al. 2006). The putative disks would have formed from fallback of supernova material (Lin, Woosley, & Bodenheimer 1991; Chatterjee, Hernquist, & Narayan 2000). Similar to an accretion disk in X-ray binaries, the dust disk is heated by the strong X-rays from the central neutron star, but since it is farther away from the central source and cooler than an accretion disk (e.g., see Hulleman et al. 2000 for the accretion disk model that was previously considered for the optical emission from 4U 0142+61), it emits mainly in the IR (Perna, Hernquist, & Narayan 2000).

⁴ See www.spitzer.caltech.edu/obs/bg.html

Using *Spitzer*/IRAC observations similar to those discussed here, the unabsorbed IR-to-X-ray flux ratio of 4U 0142+61 was found to have a maximum value of $(\nu_{4.5\mu\text{m}}F_{4.5\mu\text{m}})/F_{\text{X}} \simeq 3.4 \times 10^{-4}$ at $4.5\mu\text{m}$ (here F_{X} is phase-averaged in the 2–10 keV range, $F_{\text{X}} = 8.3 \times 10^{-11}$ ergs $\text{cm}^{-2}\text{s}^{-1}$ and $N_{\text{H}} = 0.91 \times 10^{22}\text{cm}^{-2}$; Patel et al. 2003). This ratio, as it depends largely on the geometry of the disk and not on the peculiarities of the central object, might be typical for all dust disks around young neutron stars. Thus, as a first-order hypothesis for either case, it is not unreasonable to assume that the ratio is constant from source to source, and see whether the data support this hypothesis.

In Figure 4, we show the upper limits on the mid-IR $4.5\mu\text{m}$ to X-ray unabsorbed flux ratios of the three target AXPs and compare them to the same ratio for 4U 0142+61. The unabsorbed X-ray fluxes we use are given in Table 1. Depending on the models used in spectral fitting, the resulting flux in the soft 0.5–2 keV range of the AXPs can be different by a factor of 2–3 (e.g., Tiengo et al. 2005). We therefore use the 2–10 keV unabsorbed flux, which does not change significantly for different fitting models, for comparison. As can be seen from the figure, all the upper limits are above the ratio of 4U 0142+61. (This is also true when the 0.5–10 keV X-ray fluxes are used for the comparison.) The non-detection of the sources in the mid-IR, partly because of the relatively low sensitivity limits of the *Spitzer* observations (see Table 2), could be due to their relatively low X-ray fluxes.

Our mid-IR upper limits on XTE J1810–197 set a constraint on its spectral energy distribution (SED). Its radio spectrum was found to be harder ($S_{\nu} \propto \nu^{\alpha}$, $\alpha \gtrsim -0.5$) than that of most pulsars (Camilo et al. 2006). In Figure 5, we show our dereddened upper limits with the reported fluxes from radio to X-ray energies. We used $A_V \approx 3.6$, derived from its $N_{\text{H}} = 0.65 \times 10^{22}\text{cm}^{-2}$ (Gotthelf & Halpern 2006) by using $A_V = N_{\text{H}}/(1.79 \times 10^{21}\text{cm}^{-2})$ (Predehl & Schmitt 1995), to deredden the IRAC data and MIPS datum (according to the reddening laws of Indebetouw et al. 2005 and Weingartner & Draine 2001, respectively). As can be seen, the rising radio spectrum of the source ($\alpha = -0.5$,

estimated from the radio fluxes measured nearly simultaneously) is constrained by the $4.5\mu\text{m}$ upper limit: a spectral break is thus expected to be between 4.2×10^{10} and $6 \times 10^{13}\text{Hz}$. In addition, more recently, a flux density of 1.2mJy at 144GHz (corresponding to $1.7 \times 10^{-15}\text{ergs cm}^{-2}\text{s}^{-1}$) from the source was reported (Camilo et al. 2007). This measurement further narrows the spectral break range, and may suggest a harder spectrum (e.g., $\alpha = -0.3$). However, since the AXP is highly variable in every spectral window where it has been observed and the measurements at the different frequency ranges in Figure 5 were not simultaneously obtained, the overall shape of the SED may still be highly uncertain. It is not clear whether or not the radio emission is closely related to the observed near-IR emission (see Figure 5). Even in the magnetar model, the optical/IR emission would arise from the corona of the magnetar, which is located at the closed magnetosphere region. Based on the rising radio energy spectrum, deeper observations at $\geq 24\mu\text{m}$ wavelengths, with a sensitivity comparable to the upper limit at $4.5\mu\text{m}$, are required to probe whether there is radio-related IR emission from this source. A non-detection, on the other hand, would further constrain the frequency range for the spectral break.

We thank David Kaplan and Wynn Ho for useful discussions. This research was supported by NSERC via a Discovery Grant, Steacie Supplement, and by the FQRNT and CIAR. VMK holds the Lome Trottier Chair, a Canada Research Chair and is a R. Howard Webster Foundation Fellow of the CIAR. This work is based [in part] on observations made with the Spitzer Space Telescope, which is operated by the Jet Propulsion Laboratory, California Institute of Technology under NASA contract 1407. Support for this work was provided by NASA through Contract Number 1257184 issued by JPL/Caltech. This research has made use of the data products from the Two Micron All Sky Survey, which is a joint project of the University of Massachusetts and the Infrared Processing and Analysis Center/Caltech, funded by NASA and NSF.

REFERENCES

Beloborodov, A. M. & Thompson, C. 2007, ApJ, 657, 967
 Camilo, F., Ransom, S. M., Halpern, J. P., Reynolds, J., Helfand, D. J., Zimmerman, N., & Sarkissian, J. 2006, Nature, 442, 892
 Camilo, F., et al. 2007, Submitted to ApJ, (arXiv:0705.4095)
 Chatterjee, P., Hernquist, L., & Narayan, R. 2000, ApJ, 534, 373
 Durant, M. & van Kerkwijk, M. H. 2005, ApJ, 627, 376
 —. 2006a, ApJ, 648, 534
 —. 2006b, ApJ, 650, 1070
 Fazio, G. G. et al. 2004, ApJS, 154, 10
 Gotthelf, E. V. & Halpern, J. P. 2006, in "Isolated Neutron Stars", Astrophysics & Space Science, 308, 79, (astro-ph/0608473)
 Hulleman, F., Tennant, A. F., van Kerkwijk, M. H., Kulkarni, S. R., Kouveliotou, C., & Patel, S. K. 2001, ApJ, 563, L49
 Hulleman, F., van Kerkwijk, M. H., & Kulkarni, S. 2000, Nature, 408, 689
 Indebetouw, R. et al. 2005, ApJ, 619, 931
 Israel, G. L. et al. 2003, ApJ, 589, L93
 —. 2004, ApJ, 603, L97
 Kaspi, V. M. 2007, in Isolated Neutron Stars: From the Interior to the Surface, ed. S. Zane, R. Turolla, & D. Page, Astrophysics & Space Science, 308, 1, (astro-ph/0610304)
 Lin, D. N. C., Woosley, S. E., & Bodenheimer, P. H. 1991, Nature, 353, 827
 Patel, S. K. et al. 2003, ApJ, 587, 367
 Perna, R., Hernquist, L., & Narayan, R. 2000, ApJ, 541, 344
 Predehl, P. & Schmitt, J. H. M. M. 1995, A&A, 293, 889
 Rea, N., Oosterbroek, T., Zane, S., Turolla, R., Méndez, M., Israel, G. L., Stella, L., & Haberl, F. 2005, MNRAS, 361, 710
 Rea, N. et al. 2004, A&A, 425, L5
 Rieke, G. H. et al. 2004, ApJS, 154, 25
 Skrutskie, M. F. et al. 2006, AJ, 131, 1163
 Tam, C. R., Kaspi, V. M., van Kerkwijk, M. H., & Durant, M. 2004, ApJ, 617, L53
 Thompson, C. & Duncan, R. C. 1996, ApJ, 473, 322
 Thompson, C., Lyutikov, M., & Kulkarni, S. R. 2002, ApJ, 574, 332
 Tiengo, A., Mereghetti, S., Turolla, R., Zane, S., Rea, N., Stella, L., & Israel, G. L. 2005, A&A, 437, 997
 Wang, Z. & Chakrabarty, D. 2002, ApJ, 579, L33
 Wang, Z., Chakrabarty, D., & Kaplan, D. L. 2006, Nature, 440, 772
 Weingartner, J. C. & Draine, B. T. 2001, ApJ, 548, 296

Woods, P. M. & Thompson, C. 2006, in Compact Stellar X-ray Sources, ed. W. H. G. Lewin & M. van der Klis (Cambridge: Cambridge Univ. Press), 547, (astro-ph/0406133)

TABLE 1
PROPERTIES OF 1E 1048.1–5937, 1RXS J170849.0–400910, AND XTE J1810–197

Source	P (s)	d (kpc)	$N_{\text{H}}/10^{22}$ (cm^{-2})	F_{X}^{a} $/10^{-11}$ ($\text{ergs cm}^{-2} \text{ s}^{-1}$)	Adopted Position ^b	Refs
1E 1048.1–5937	6.4	8.6	1.0	0.74	$10^{\text{h}} 50^{\text{m}} 07\rlap{.}^{\text{s}} 13 -59^{\circ} 53' 21\rlap{.}^{\text{s}} 3$	1–3
1RXS J170849.0–400910	11.0	3.8	1.38	2.4	$17^{\text{h}} 08^{\text{m}} 46\rlap{.}^{\text{s}} 90 -40^{\circ} 08' 52\rlap{.}^{\text{s}} 64$	2,4,5
XTE J1810–197	5.5	3.3	0.65	0.10	$18^{\text{h}} 09^{\text{m}} 51\rlap{.}^{\text{s}} 08 -19^{\circ} 43' 51\rlap{.}^{\text{s}} 74$	6–8

REFERENCES. — (1) Tiengo et al. (2005); (2) Durant & van Kerkwijk (2006b); (3) Wang & Chakrabarty (2002); (4) Rea et al. (2005); (5) Israel et al. (2003); (6) Gotthelf & Halpern (2006); (7) Israel et al. (2004); (8) Camilo et al. (2006).

NOTE. — X-ray observations made at epochs close to the epochs of our *Spitzer*/IRAC observations (see Table 2) are used. The X-ray fluxes of 1E 1048.1–5937, 1RXS J170849.0–400910, and XTE J1810–197 were measured on 2004 July 08 (Tiengo et al. 2005), 2003 Aug 28 (Rea et al. 2005), and 2005 Sep 20 (Gotthelf & Halpern 2006), respectively.

^a Unabsorbed, phase-averaged 2–10 keV X-ray flux.

^b Source positions are all J2000.0, and have a 90% uncertainty of $0\rlap{.}^{\prime\prime} 5$ for 1E 1048.1–5937 and $0\rlap{.}^{\prime\prime} 7$ for 1RXS J170849.0–400910 and XTE J1810–197.

TABLE 2
Spitzer IMAGING OBSERVATIONS OF THREE AXPs AT 4.5, 8.0, AND 24 μ M

Object	Date	Instrument	Exposure (min)			Sky Brightness (MJy/sr)			Flux upper limit (mJy)		
			4.5	8.0	24	4.5	8.0	24	4.5	8.0	24
1E1048 ^a	2005-06-13	IRAC	16.3	15.8	...	0.52	10	...	0.008	0.041	...
	2005-04-02	MIPS	7.2	37	0.39
J1708 ^a	2005-08-24	IRAC	16.3	15.8	...	3.1	63	...	0.12	0.17	...
	2005-04-12	MIPS	7.2	62	0.59
J1810 ^a	2005-09-22	IRAC	32.4	31.4	...	2.4	77	...	0.023	0.13	...
	2005-04-13	MIPS	7.2	86	0.88

^a Full names are 1E 1048.1–5937, 1RXS J170849.0–400910, and XTE J1810–197.